

Dynamic Modulation of Electronic and Optical Properties in GaN Bilayers by Interlayer Sliding

Heeju Kim and Gunn Kim*

*Department of Physics & Astronomy and Hybrid Materials Research Center, Sejong University, Seoul 05006,
Republic of Korea*

*Corresponding author: gunnkim@sejong.ac.kr

Abstract

In this study, we present a first-principles investigation of the electronic and optical properties of gallium nitride (GaN) bilayers, focusing on the influence of interlayer sliding and spacing. In contrast to the earlier studies on discrete stacking configurations, we explore the dynamic evolution of the properties during transitions between stable stacking arrangements. Using density functional theory calculations, we systematically analyze the impact of these structural variations on the electronic band structure and optical absorption spectra of GaN bilayers. The analysis includes both high-symmetry stacking configurations (AA', AB', and AC') and intermediate states generated by controlled in-plane atomic displacements, thereby providing a comprehensive understanding of the property changes associated with interlayer sliding. The findings of this study provide valuable insights into the potential for tuning the electronic and optical response of two-dimensional GaN for applications in nanoscale photonic and electronic devices, where precise control over interlayer interactions and stacking is crucial.

Keywords: two-dimensional gallium nitride (2D GaN), density functional theory, electronic structures, optical properties, ab initio molecular dynamics simulation

1. Introduction

Gallium nitride (GaN) is a wide-bandgap semiconductor with a direct bandgap of approximately 3.4 electronvolts (eV) [1, 2]. This material has had a profound effect on the fields of optoelectronics and high-power electronics. Its superior properties compared to silicon, including efficient light emission and high breakdown voltage, have enabled breakthroughs in blue/ultraviolet light-emitting diodes (LEDs) [3, 4], laser diodes (LDs) [5, 6], and high-electron-mobility transistors (HEMTs) [7-9]. The applications include solid-state lighting [10, 11], power conversion [12, 13], and 5G/6G communication [14, 15]. Typically crystallizing in the wurtzite structure, GaN exhibits inherent anisotropy, giving rise to piezoelectric [16] and polar characteristics [17] that are crucial for various device functionalities.

The advent of two-dimensional (2D) materials, exemplified by graphene [18], hexagonal boron nitride (h-BN) [19-21], and transition metal dichalcogenides (TMDs) [22-25], has opened unprecedented opportunities for tailoring material properties through quantum confinement and surface effects. This dimensional reduction has inspired intense research on 2D GaN [26-28], aiming to harness its unique potential for next-generation nanoscale devices. While bulk GaN has proven to be a highly effective material in numerous applications, its inherent limitations with respect to miniaturization and integration with flexible substrates have prompted intensive research into its 2D counterparts. Notably, theoretical studies have predicted diverse structural phases of 2D GaN, including wurtzite, haeckelite, and hexagonal structures, depending on the number of layers and stacking order [29]. The findings emphasize the material's structural adaptability and the emergence of novel properties distinct from bulk GaN. This structural polymorphism offers a promising avenue for tuning the electronic and optical properties of GaN for advanced device applications. However, the dynamic interplay

between interlayer stacking and electronic/optical properties during sliding remains poorly understood.

This study addresses this critical gap by investigating the dynamic modulation of electronic and optical properties in GaN bilayers induced by interlayer sliding. Focusing on hexagonal bilayer GaN, we consider three representative stacking configurations—AA', AB', and AC'—that naturally arise without rotational disorder. Using first-principles density functional theory (DFT) calculations, we systematically analyze the evolution of electronic band structures and optical absorption spectra as a function of interlayer sliding. This approach enables the discernment of the intricate relationship between interlayer interactions, electronic structure, and optical response, thereby providing insights into the dynamic tunability of 2D GaN. Unlike previous studies that primarily focused on static stacking configurations [30, 31], our work explores the dynamic transitions between these configurations, thereby offering a more comprehensive understanding of the structure-property relationships in 2D GaN bilayers. The findings provide valuable guidelines for the design and optimization of future nanoscale photonic and electronic devices based on 2D GaN, where precise control over interlayer interactions and stacking is important.

2. Computational Details

We investigated the interlayer interactions of GaN bilayers using first-principles calculations based on density functional theory (DFT), as implemented in the Vienna *Ab initio* Simulation Package (VASP) [32-34]. The exchange-correlation functional was treated within the generalized gradient approximation (GGA) using the Perdew-Burke-Ernzerhof (PBE)

parameterization [35]. Core-valence interactions were described by the projector augmented-wave (PAW) method [34, 36], with a plane-wave basis set and a kinetic energy cutoff of 650 eV. Structural relaxations were performed until residual forces on all atoms were less than 0.01 eV/Å and the total energy converged to within 10^{-6} eV. To minimize spurious interactions between periodic images in the non-periodic z -direction, a vacuum spacing of at least 15 Å was employed. A $15 \times 15 \times 1$ k -point mesh was used for structural relaxations and electronic structure calculations, while a denser $30 \times 30 \times 1$ mesh was employed for optical property calculations. Interlayer van der Waals interactions were accounted for using Grimme's DFT-D3 correction [37, 38]. The VASPKIT toolkit [39] was used for post-processing and analysis of the calculated data.

The structural stability of the GaN monolayer and bilayers was validated by *ab initio* molecular dynamics (AIMD) simulations (Figure S1, Supplementary Materials). *NVT* ensemble simulations were performed at 300 K, 400 K, and 500 K with a 1 fs time step and a total simulation time of 5 ps (5000 steps). The observed stability of the total energy profiles over the temperature range confirms the suitability of these structures for further DFT analysis.

3. Results and Discussion

3.1 Structural properties

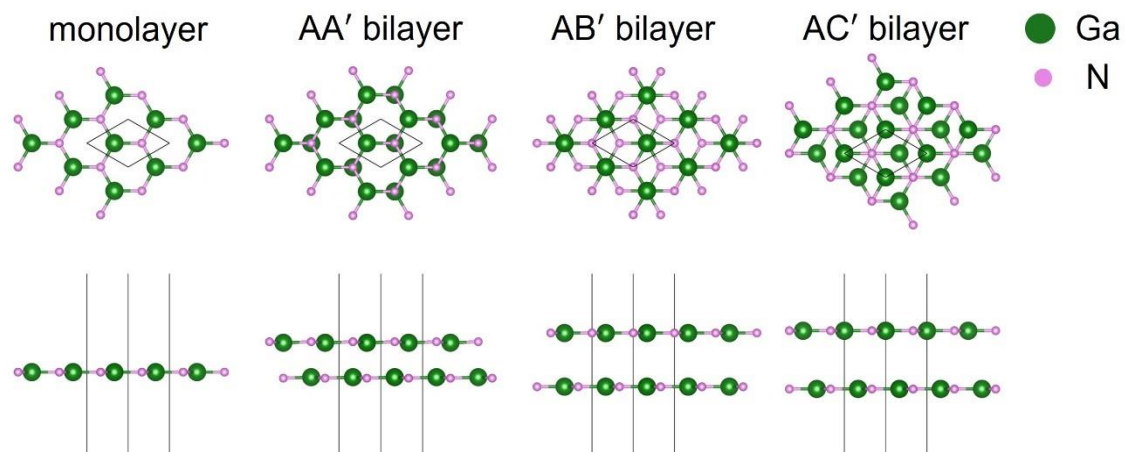


Figure 1. Top and side views of a monolayer and AA', AB', and AC' stacked GaN bilayers. Ga and N atoms are represented by green and pink spheres, respectively. Unit cells are outlined by black lines.

We first investigated the structural properties of monolayer and bilayer GaN. Figure 1 shows the top and side views of the considered structures: monolayer, AA', AB', and AC' bilayers. All structures adopt a planar hexagonal lattice similar to that of hexagonal boron nitride (h-BN). The AA' stacking configuration consists of two perfectly aligned hexagonal layers, where atoms of the same species in the top and bottom layers are directly superimposed. This AA' stacking is found to be the most energetically favorable configuration. In the AB' stacking, the Ga atoms of the two layers are vertically aligned, resulting in the N atoms occupying the hollow sites of the opposing layer. In contrast, in AC' stacking, the N atoms are vertically aligned, with the Ga atoms occupying the hollow sites of the opposing layer.

Table 1. Structural properties of the GaN monolayer and bilayers.

	in-plane lattice constant (Å)	bond length (Å)	bond angle (°)	interlayer distance (Å)
monolayer	3.206	1.851	120.0	-
AA' bilayer	3.266	1.887	119.9	2.394
AB' bilayer	3.204	1.850	120.0	3.594
AC' bilayer	3.204	1.850	120.0	3.913

Table 1 summarizes the key structural parameters of the considered GaN configurations. The in-plane lattice constant of the monolayer is calculated to be 3.206 Å. In the AA'-stacked bilayer, the in-plane lattice constant expands to 3.266 Å, indicating a measurable influence of interlayer interactions. The results are in good agreement with previous studies [40]. This expansion is accompanied by an increase in the in-plane Ga-N bond length from 1.851 Å in the monolayer to 1.887 Å in the AA' bilayer. The bond angle remains nearly unchanged, with a value of 119.9° in the AA' bilayer compared to 120.0° in the monolayer. The relatively short interlayer distance in the AA' configuration (2.394 Å) suggests a significant interlayer interaction, stronger than typical van der Waals interactions, approaching a weak chemical bonding regime. This strong interlayer coupling is also manifested in the observed structural buckling of the AA' bilayer, with an out-of-plane displacement of 6.9 pm between the Ga and N atoms within each layer. This buckling is a direct consequence of the interlayer interactions and distinguishes the AA' bilayer from the planar monolayer structure.

In contrast, the AB' and AC' bilayers exhibit significantly larger interlayer distances of 3.594 Å and 3.913 Å, respectively. These larger separations suggest weaker interlayer

interactions, which is reflected in their in-plane lattice constants (3.204 \AA) and Ga-N bond lengths (1.850 \AA) being much closer to those of the monolayer. It means that interlayer interactions have a negligible effect on the in-plane structural parameters in the configurations, likely due to the increased interlayer spacing. Furthermore, the observed trend indicates that as the interlayer separation increases and the interlayer coupling weakens, the structural parameters of the bilayer converge to those of an isolated monolayer.

The difference in interlayer spacing between the AB' and AC' stackings is due to the interplay of electrostatic repulsion resulting from the specific atomic arrangements. In the AC' stacking, the nitrogen atoms face each other across the layers. Since nitrogen is highly electronegative, the close proximity of these negatively charged nitrogen atoms results in significant electrostatic repulsion. This repulsion pushes the layers further apart, resulting in a larger interlayer distance. Conversely, in AB' stacking, gallium atoms face each other. Gallium is less electronegative than nitrogen, meaning that the electrostatic repulsion between gallium atoms is weaker than that between nitrogen atoms in the AC' stacking.

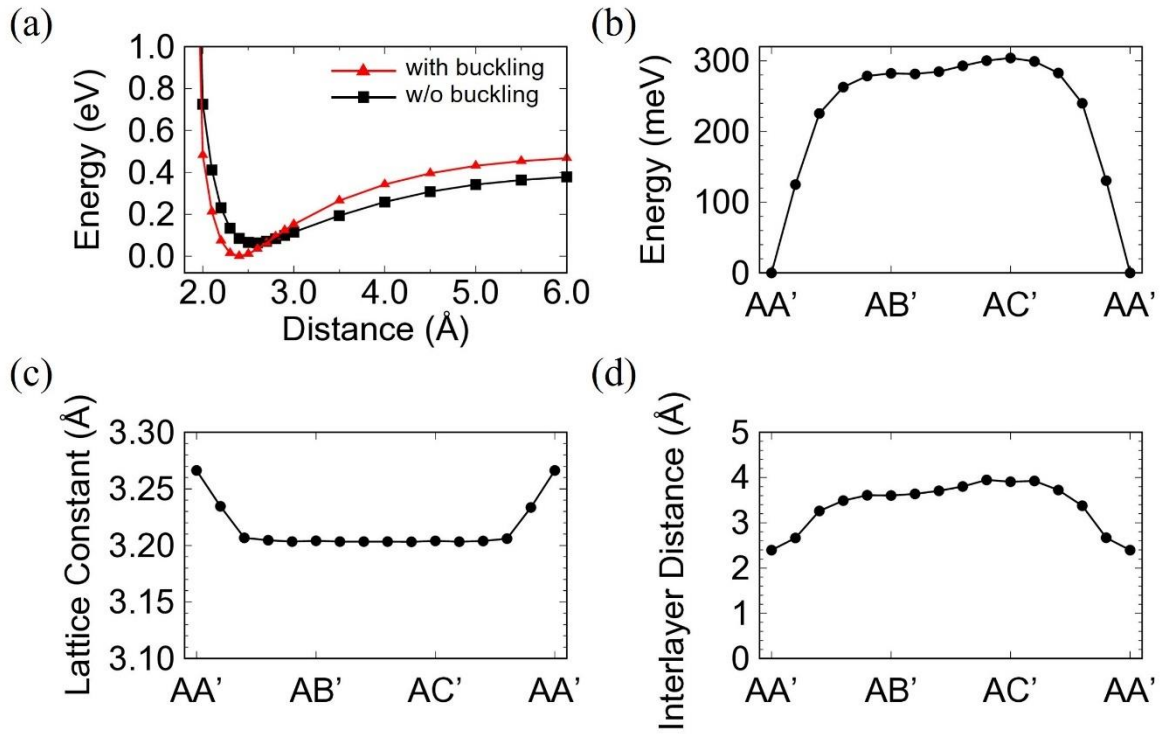


Figure 2. (a) Total energy of the AA' bilayer as a function of interlayer distance, with and without buckling. (b) Relative energy, (c) in-plane lattice constants, (d) interlayer distances during the sliding process.

Next, we analyzed the energetics and structural evolution during interlayer sliding. Figure 2(a) shows the total energy of the AA' bilayer as a function of interlayer distance, comparing buckled and unbuckled configurations. As the interlayer distance decreases from large separations, the total energy decreases due to increasing attractive interlayer interactions, primarily van der Waals forces. However, at short interlayer distances, strong repulsive forces arise due to Pauli repulsion, leading to a rapid increase in energy. The buckled configuration reaches its minimum energy at an interlayer distance of 2.4 \AA , which is 64 meV lower than the minimum energy of the unbuckled configuration at 2.6 \AA . This energetic preference for the buckled structure suggests that the buckling stabilizes the bilayer by optimizing the interlayer

bonding environment. The crossing of the two energy curves at $\sim 2.7\text{-}2.8 \text{ \AA}$ indicates a transition from a buckled to an unbuckled ground state. Beyond this distance, the unbuckled structure becomes energetically more favorable, asymptotically approaching the energy of two independent monolayers as interlayer interactions vanish.

Figure 2(b) presents the energy profile during the sliding transitions from the AA' stacking to the AB' and AC' stackings, with the energy of the AA' configuration set to zero. The AB' and AC' stackings are found to be 282 meV and 304 meV higher in energy than the AA' stacking, respectively, indicating their relative instability. The steep energy gradients observed during the AA' \rightarrow AB' and AC' \rightarrow AA' transitions suggest significant energy barriers and a strong driving force for the system to relax back to the AA' configuration. In contrast, the relatively gentle slope of the AB' \rightarrow AC' transition implies a lower energy barrier for this pathway. Notably, a local minimum, approximately 1 meV lower in energy than the AB' configuration, is observed at a displacement slightly beyond the AB' stacking. This local minimum may correspond to a metastable intermediate state during the AB' \rightarrow AC' transition.

The changes in in-plane lattice constants and interlayer distances during these transitions are shown in Figures 2(c) and 2(d), respectively. The in-plane lattice constant exhibits a maximum value at the AA' stacking and its neighboring points, with a variation of approximately 6.3 pm over all configurations. The interlayer distance increases monotonically from the AA' (2.394 \AA) to the AB' (3.602 \AA) and AC' (3.907 \AA) stackings, which is in good agreement with the weakening of interlayer interactions and the increasing energetic instability. The influence of the structural changes on the electronic properties, including the electronic band structure and partial density of states (PDOS), will be discussed in the following section.

3.2 Electronic structures

We now turn to the electronic properties of the 2D GaN structures, analyzing both the evolution of the band structure with varying interlayer spacing and the changes induced by interlayer sliding. Figure 3 presents the electronic band structures and density of states (DOS) for the monolayer and the three bilayer stacking configurations (AA', AB', and AC'). The Fermi level is set to 0 eV as the reference energy.

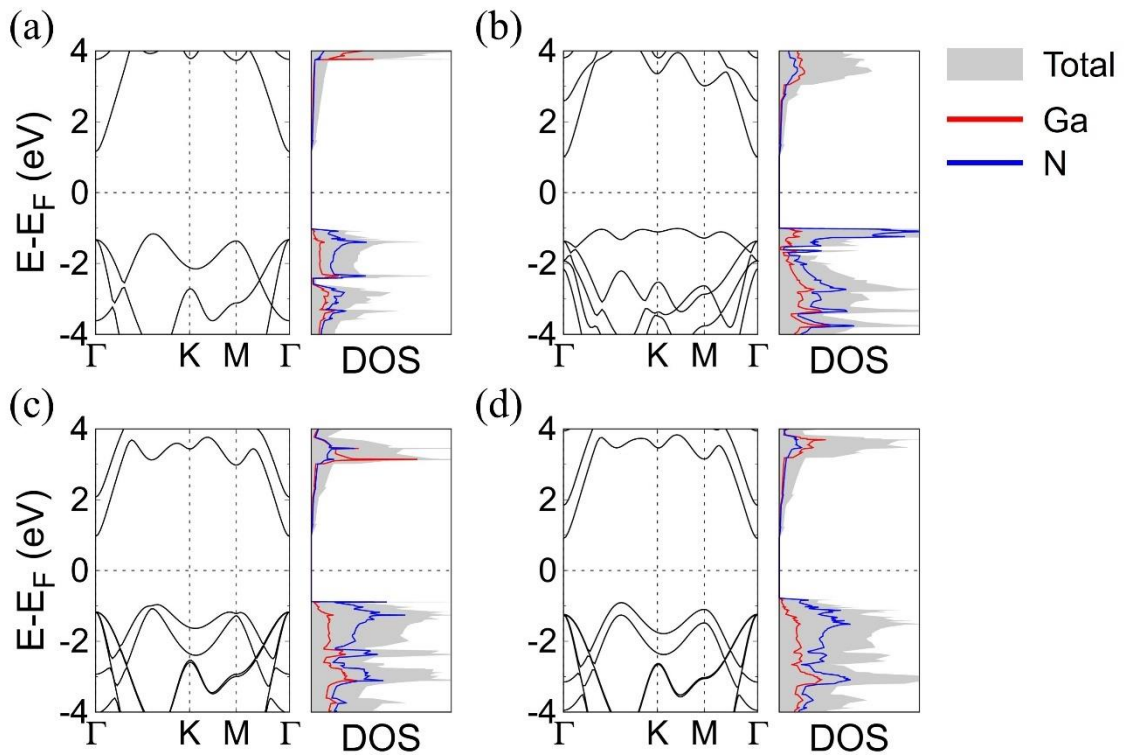


Figure 3. Electronic band structures (left panels) and density of states (DOS; right panels) for (a) monolayer, (b) AA' bilayer, (c) AB' bilayer, and (d) AC' bilayer GaN. The Fermi level (E_F) is set to 0 eV. In the DOS plots, the gray shaded area represents the total DOS, while red and blue lines represent the projected DOS (PDOS) for Ga and N atoms, respectively.

The calculated indirect band gaps for the monolayer, AA', AB', and AC' bilayers are 2.32 eV, 2.03 eV, 1.93 eV, and 1.81 eV, respectively. The decrease in band gap upon bilayer formation is a direct consequence of interlayer coupling, which leads to splitting of both the valence and conduction bands. This splitting results from the interaction between the electronic states of the two layers, resulting in bonding and antibonding states. The energy difference between the bonding and antibonding states determines the change in band gap. The magnitude of this splitting, and the band gap value, is further modulated by the specific stacking arrangement. In the monolayer in Figure 3(a), the highest valence band, composed mainly of nitrogen p-orbitals, exhibits a larger dispersion. For the AA'-stacked bilayer in Figure 3(b), this band splits into two due to interlayer hybridization. One of the two bands remains close to the valence band maximum (VBM), approximately at -1 eV, while the other shifts to lower energies, ranging from -2 eV to -3 eV. In particular, the highest valence band in the AA' bilayer becomes almost flat (even less dispersive). This reduced dispersion is directly reflected in the DOS plot, where the peak near the VBM becomes sharper and more pronounced, indicating a higher DOS. The flattening of the VBM in the AA' bilayer, reflected in the sharp and pronounced peak near the VBM in the DOS, indicates a localization of the hole states. This localization implies an increase in the effective mass of a hole and consequently a reduction in hole mobility, which is expected to negatively affect the hole conductivity of the material.

The electronic structures of the AB' and AC' bilayers, shown in Figure 3(c) and (d), are generally similar to the monolayer, indicating weaker interlayer coupling compared to the AA' configuration. This weaker coupling is evident in the smaller splitting of the valence bands near the VBM compared to the AA' bilayer. However, considerable differences are also observed,

particularly in the behavior of the bands near the VBM and conduction band minimum (CBM).

In both the AB' and AC' configurations, the uppermost valence band splits into two, as observed in the AA' bilayer. However, unlike the AA' configuration where one of these bands becomes nearly flat, both bands in AB' and AC' retain a significant degree of dispersion, similar to the monolayer. This indicates that the hole states in AB' and AC' are less localized compared to the AA' configuration, suggesting higher hole mobilities. A key difference between AB' and AC' lies in the relative positions of these two split bands. In the AB' stacking, these two bands cross between the Γ and K points, as well as at the M point, indicating a change in the character of the valence band states at these points. This crossing is likely due to a specific combination of interlayer and intralayer orbital interactions resulting from the AB' stacking, leading to a different hybridization pattern compared to the AA' stacking. This band crossing could lead to interesting transport properties. In contrast, the AC' stacking shows a more uniform separation between the two bands, with no crossing observed. This difference can be attributed to the different relative positions of the atoms in the two layers, which affects the overlap between the orbitals and thus the strength of the interaction.

In addition, a notable feature observed in both AB' and AC' bilayers, and different from the monolayer, is the downward shift of the band just above the lowest conduction band at the Γ point. This band shifts down to about +2 eV (relative to the Fermi level) in both AB' and AC', whereas it is at higher energies in the monolayer. This shift is probably a consequence of the interlayer interaction, although it is weaker than in the AA' configuration. This change in the conduction band structure could also affect the electron transport properties.

The DOS plots of the AB' and AC' bilayers show a doubling of the overall DOS compared to the monolayer, as expected for a bilayer system. However, subtle differences are observed in the PDOS. In the AB' stacking, the Ga peak near +3 eV is sharper and narrower compared to the AC' stacking. This indicates a higher density of Ga-related states at this energy and, importantly, a tendency to localize the states. This localization implies an increase in the electron effective mass and consequently a decrease in the electron mobility at this energy.

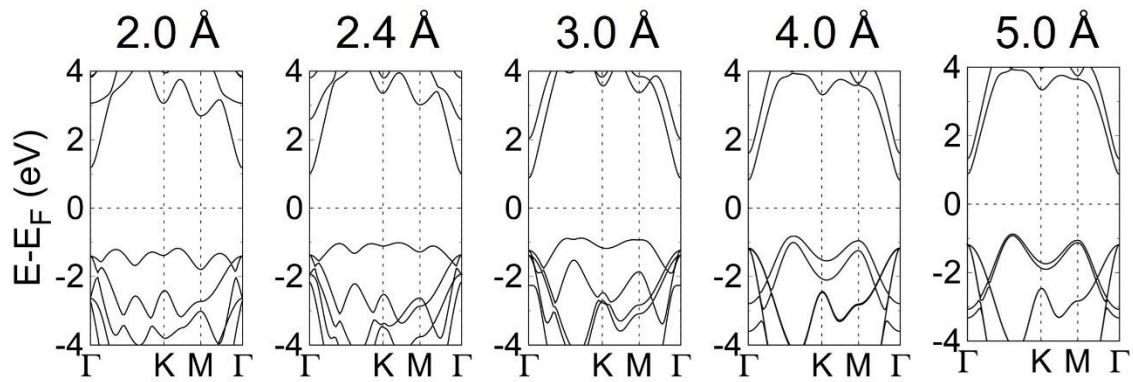


Figure 4. Electronic band structures of AA'-stacked GaN bilayers as a function of interlayer distance. The interlayer distance (in Å) is indicated above each band structure. The equilibrium interlayer distance is 2.4 Å.

We then studied the evolution of the topmost valence band in the AA' bilayer as a function of interlayer separation. At large separations, the bilayer effectively behaves as two independent monolayers, exhibiting a band structure characteristic of isolated layers. This means that the bands are more dispersive, reflecting the electronic structure of the individual

layers. As the layers approach each other, the increasing interlayer coupling modifies the band structure, especially near the VBM.

Figure 4 shows the evolution of the electronic band structure of the AA'-stacked bilayer as a function of interlayer distance. At a large spacing of 5.0 \AA , the band structure closely resembles that of the monolayer, with a dispersive topmost valence band. Systematic changes occur as the interlayer spacing decreases. Near the Γ point, the topmost valence band progressively flattens, indicating the onset of interlayer hybridization and the formation of bonding and antibonding states. This flattening is most pronounced at the equilibrium interlayer spacing of 2.4 \AA , corresponding to optimal interlayer electronic coupling and strong hole localization. However, at a compressed interlayer spacing of 2.0 \AA , the band structure undergoes a significant transformation. The previously flattened valence band regains dispersion, and the overall band structure becomes more complex, deviating markedly from both the monolayer and equilibrium bilayer configurations. This behavior suggests that at such short interlayer distances, strong interatomic repulsion dominates, leading to significant changes in orbital hybridization and the formation of distinct electronic states.

Importantly, the behavior of the band immediately below the top valence band (initially at -3 to -2 eV) provides further insight into the interlayer interaction. At large interlayer separations (e.g., 5.0 \AA), this band shifts upward in energy and approaches the topmost valence band, showing a tendency toward degeneracy. This near-degeneracy at larger separations is a consequence of the weakened interlayer coupling. As the layers become further apart, their electronic states become less perturbed by each other and converge toward the independent monolayer limit. Therefore, the near-merging of the bands at 5.0 \AA indicates a decoupling of

the layers. As the interlayer distance decreases from 5.0 Å towards the equilibrium value, this band moves further away from the top valence band, indicating a strengthening of the interlayer interaction. This increased splitting between the bands reflects the formation of distinct bonding and antibonding states due to the enhanced interlayer coupling.

The band structure also evolves during interlayer sliding between different stacking configurations (AA'→AB'→AC'→AA' in Figure S2). As shown in Figure 3, significant differences in the band structures are observed during the AA'→AB' and AC'→AA' transitions. Figure S2 shows how the flat band characteristic of the AA' configuration is modified during these transitions. The observed band changes during sliding are qualitatively similar to those seen with varying interlayer distance in Figure 4. This suggests that the AB' and AC' stackings can be conceptually understood as representing states with larger effective interlayer distances compared to the stable AA' configuration, although the specific atomic arrangements and resulting orbital interactions also play a crucial role in determining the precise electronic structure. The band gap change during the transitions is shown in Figure S3.

3.3 Optical properties

We now turn to the optical properties of 2D GaN. The dielectric function, which describes the interaction of the material with light, is critical to understand its optical behavior. The dielectric function is a complex quantity, expressed as:

$$\varepsilon(\omega) = \varepsilon_1 + i\varepsilon_2 \quad (1)$$

where ε_1 and ε_2 represent the real and imaginary components, respectively. The in-plane symmetry of the 2D GaN structures leads to a diagonal dielectric tensor with equal in-plane

components ($\epsilon_{xx} = \epsilon_{yy}$) and zero off-diagonal components. Consequently, the optical response in the plane is isotropic. We thus focus on the real and imaginary parts of ϵ_{xx} in Figure 5(a) and ϵ_{zz} in Figure 5(b), respectively.

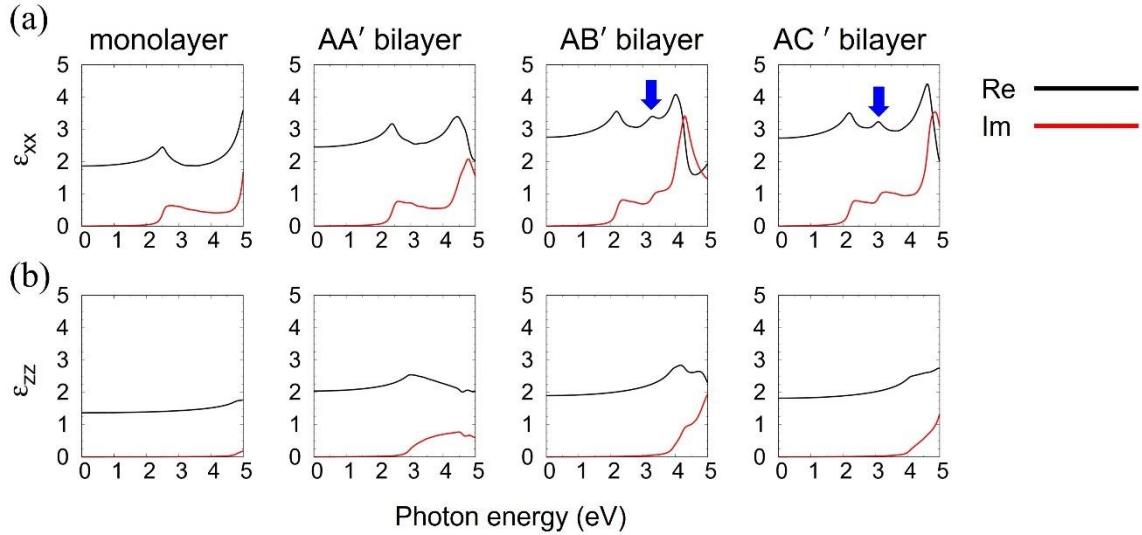


Figure 5. (a) In-plane (ϵ_{xx}) and (b) out-of-plane (ϵ_{zz}) components of frequency-dependent dielectric functions of GaN monolayer, AA', AB', AC' stacking bilayers. The black and red solid lines represent the real and imaginary parts of the function, respectively.

Figures 5(a) and 5(b) shows the frequency-dependent dielectric functions for the monolayer and various bilayer configurations, plotted as a function of photon energy for both the in-plane (ϵ_{xx}) and out-of-plane (ϵ_{zz}) components, respectively. Each graph presents the real (ϵ_1 , black line) and imaginary (ϵ_2 , red line) parts of the dielectric function. We first focus on the in-plane dielectric function (ϵ_{xx}) shown in Figure 5(a).

Looking at ϵ_1 , the monolayer exhibits a prominent peak around 2.5 eV, followed by a relatively flat region before a sharp increase at ~ 5.0 eV. This indicates that electronic transitions

in the monolayer are concentrated in certain energy regions, with a significant transition occurring at higher energies. In the AA' stacking bilayer, the first peak is observed at about 2.4 eV, close to that of the monolayer. However, there is a significant difference in the position of the second peak, which is shifted to approximately 4.4 eV, occurring at a lower energy than the monolayer peak at ~5.0 eV. This shift implies that the interlayer interaction in the AA' stacking significantly modifies the electronic structure, leading to electronic transitions at different energies.

The AB' and AC' stacking bilayers exhibit three distinct peaks/humps in ϵ_1 , unlike the two peaks observed in the monolayer and AA' stacking. The first peaks for the AB' (~2.2 eV) and AC' (~2.2 eV) configurations are located near the first peaks of the monolayer and AA' configurations. Notably, both AB' and AC' exhibit a second hump/shoulder, indicated by arrows in Figure 5(a), that is absent in the monolayer and AA' stacking. This second hump/shoulder is located at ~3.3 eV for AB' and ~3.1 eV for AC'. The presence of this additional hump/shoulder suggests more complex interlayer interactions in the configurations, enabling additional electronic transitions. The third peaks in the AB' (~4.0 eV) and AC' (~4.6 eV) stackings are also shifted to lower energies compared to the second peak of the monolayer at ~5.0 eV.

Turning to the imaginary part (ϵ_2) of ϵ_{xx} (red line) in Figure 5(a), we observe similar trends across the configurations, although the features are less distinct than in the real part. In the monolayer, the main absorption peak occurs at ~ 5.1 eV, indicating strong optical absorption at this energy. The AA' stacking bilayer exhibits a lower energy peak at ~4.8 eV, which corresponds to the shifted peak observed in the real part (ϵ_1), further confirming the influence

of interlayer coupling. In the AB' and AC' configurations, the highest absorption peaks are observed at ~4.3 eV and ~4.9 eV, respectively. Similar to the real part, both AB' and AC' exhibit an additional feature ~3.4 eV for AB' and ~3.3 eV for AC', which can be described as a hump/shoulder and is absent in the monolayer and AA' stacking. The extra features suggest that the AB' and AC' stackings introduce new electronic transitions, likely due to their distinct interlayer interactions and resulting asymmetry.

Figure 5(b) shows the out-of-plane component (ϵ_{zz}) of the dielectric function. The monolayer exhibits a nearly flat response, particularly in the real part (ϵ_1), with minimal variation across the photon energy range. This behavior is expected for a monolayer material, where the electronic structure is predominantly confined within the 2D plane. Since there is no interlayer coupling in a monolayer, electronic transitions polarized along the out-of-plane direction are significantly suppressed, resulting in a nearly constant dielectric response. In contrast, the bilayer structures show more pronounced variation in the ϵ_{zz} component, especially above 3 eV in the ultraviolet region. This increased response is attributed to the introduction of interlayer coupling, which enables additional electronic transitions polarized along the out-of-plane direction that are absent in the monolayer.

Interestingly, the imaginary part (ϵ_2) of ϵ_{zz} exhibits distinct behavior among the bilayer stackings. While the ϵ_2 curve of the AA' stacking appears to saturate around 4-5 eV, the ϵ_2 curve of the AB' and AC' stackings continues to increase in this energy range. This difference indicates that the AB' and AC' stackings possess additional out-of-plane electronic transitions at higher energies compared to the AA' stacking, likely due to their different interlayer configurations and resulting changes in the out-of-plane electronic structure. This increased

out-of-plane response in AB' and AC' contributes to the overall optical anisotropy of these bilayers. The optical properties including 2D conductivity and optical absorptivity, transmissivity, and reflectivity are obtained from the dielectric functions and shown in Figure S4.

To further understand the origin of the observed optical features, we calculated the transition dipole moments (TDMs). The sum of the squares of the TDMs provides a measure of the transition probabilities between valence and conduction bands. Our calculations reveal that the most significant transitions occur near the Γ point. Comparing the bilayer configurations, we find that the squared TDM for the transition from the valence band at Γ to the conduction band at Γ is largest in the AA' bilayer. This strong transition explains the prominent first peak observed in the in-plane dielectric function (ϵ_{xx}) of the AA' bilayer, as shown in Figure 5(a). In the AB' and AC' structures, this transition from the VBM to the CBM at Γ also exhibits a large squared TDM, contributing to their respective first peaks. However, a key difference emerges in the AB' and AC' configurations: we observe a significant transition probability from the VBM at Γ to the second lowest conduction band at Γ . This additional transition, which is absent in the monolayer and AA' stacking, accounts for the second hump/shoulder observed in the ϵ_{xx} spectra of the AB' and AC' configurations indicated by blue arrows in Figure 5(a). This finding directly links the observed optical features to specific electronic transitions enabled by the distinct interlayer interactions and resulting electronic structures of the AB' and AC' stackings.

The influence of interlayer interactions on the optical properties was also examined. Figure S5 depicts the changes in the in-plane component of the frequency-dependent dielectric

function (ϵ_{xx}) as the interlayer distance is varied relative to the stable AA' configuration. When the interlayer distance is at or below the equilibrium value, the real and imaginary parts of ϵ_{xx} exhibit two prominent features, one in the 2-3 eV range and another in the 4-5 eV range. However, as the interlayer spacing increases beyond the equilibrium separation, the higher-energy feature undergoes a splitting, forming two distinct peaks. As the layers are further separated, one of these split peaks shifts progressively towards lower energies, eventually merging with the lower-energy feature near 2 eV at a separation of 5 Å. This evolution of the dielectric function clearly illustrates the significant role of interlayer interactions in determining the optical response, resulting in a pronounced shift of spectral features with varying interlayer distance.

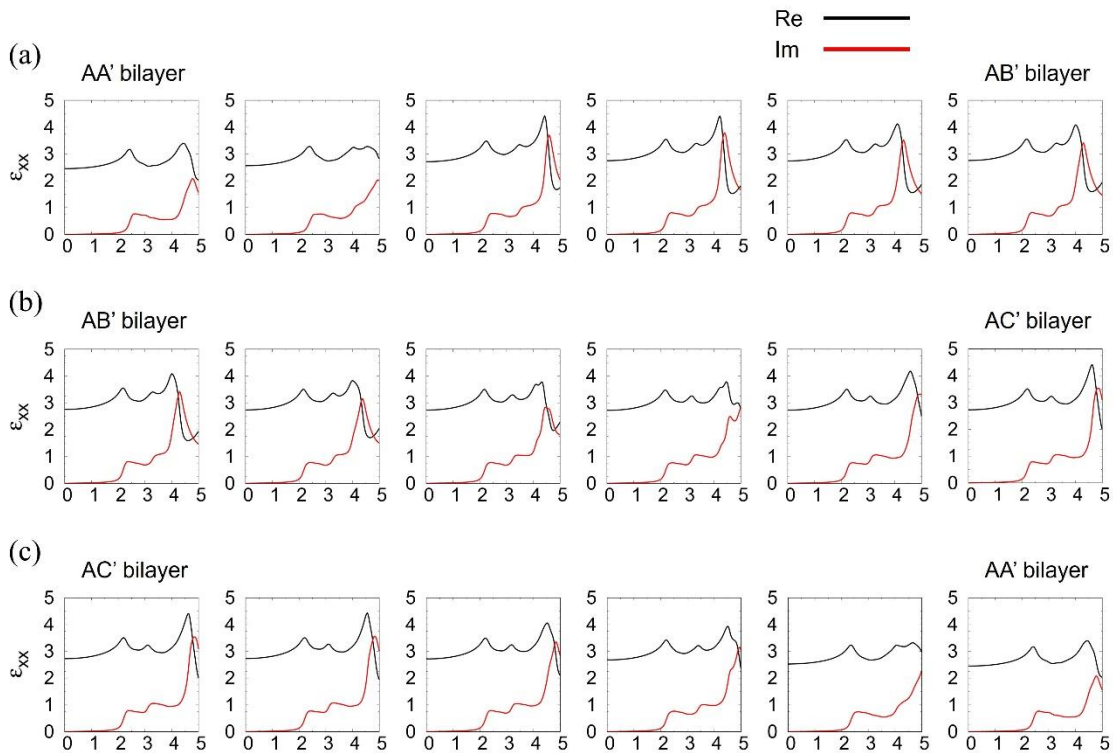


Figure 6. The in-plane component of the frequency-dependent dielectric function (ϵ_{xx}) as a result of sliding in bilayers. (a) represents sliding process AA' \rightarrow AB', (b) AB' \rightarrow AC', and (c) AC' \rightarrow AA'. The black and red lines indicate the real and imaginary parts,

respectively.

Figure 6 presents the evolution of the in-plane dielectric function (ϵ_{xx}) during interlayer sliding in the bilayers. For the AA' \rightarrow AB' transition as shown in Figure 6(a), the higher-energy feature around 4-5 eV splits into two distinct peaks. Figure 6(b) depicts the AB' \rightarrow AC' transition, where the imaginary part exhibits a decrease in peak intensity at the midpoint of the sliding path, followed by a subsequent increase as the configuration approaches AC'. Figure 6(c) shows the AC' \rightarrow AA' transition, which exhibits a behavior similar to the reverse of the AA' \rightarrow AB' transition, retracing the changes observed in Figure 6(a).

4. Conclusion

In this study, we investigated the structural, electronic, and optical properties of GaN bilayers, focusing on the influence of stacking configurations (AA', AB', and AC') and interlayer spacings and sliding. By analyzing static configurations and intermediate stages during sliding transitions and interlayer spacing variations, we elucidated the intricate interplay between these parameters and the behavior of the material. Our structural analysis revealed that the AA' stacking is the most stable configuration, exhibiting significant interlayer interactions that induce structural buckling, a feature absent in the less stable AB' and AC' stackings. The properties of the AB' and AC' stackings increasingly resemble those of two weakly interacting monolayers, demonstrating the essential role of interlayer coupling in determining bilayer properties.

Electronic structure analysis revealed a correlation between structural stability and band gap: less stable stackings exhibit smaller band gaps. In particular, the strong interlayer coupling in the AA' stacking leads to a pronounced flattening of the uppermost valence band, which directly affects the hole transport properties and demonstrates the potential for tuning the electronic properties of GaN bilayers for nanoscale electronic applications.

Our optical property analysis further highlighted the sensitivity of GaN optical response to stacking configuration and interlayer distance. The AA' stacking displayed distinct optical signatures. Importantly, the emergence of additional optical transitions in the AB' and AC' configurations, attributed to their distinct interlayer interactions, opens up new possibilities for tailoring the optical response of GaN. This tunability, achieved through the manipulation of stacking arrangements and interlayer spacing, presents significant opportunities for designing advanced photonic and optoelectronic devices.

This study establishes a comprehensive framework for understanding and exploiting the tunability of GaN bilayers through stacking and interlayer engineering. By demonstrating the profound influence of these parameters on both electronic and optical properties, our findings provide valuable insights into the design of advanced two-dimensional materials and pave the way for the design of GaN-based devices with tailored functionalities, including high-performance transistors, photodetectors, and light-emitting diodes, achieved through precise control over interlayer interactions.

Acknowledgements

This research was supported by the Basic Science Research Program through the National Research Foundation of Korea (NRF) funded by the Ministry of Education (NRF-2020R1A6A1A03043435).

References

- [1] M. Rais-Zadeh, V.J. Gokhale, A. Ansari, M. Faucher, D. Théron, Y. Cordier, L. Buchaillot, Gallium nitride as an electromechanical material, *Journal of Microelectromechanical Systems*, 23 (2014) 1252-1271.
- [2] R. Schwarz, K. Khachatryan, E. Weber, Elastic moduli of gallium nitride, *Appl. Phys. Lett.*, 70 (1997) 1122-1124.
- [3] S. Nakamura, M.R. Krames, History of gallium–nitride-based light-emitting diodes for illumination, *Proc. IEEE*, 101 (2013) 2211-2220.
- [4] S. Rajbhandari, J.J. McKendry, J. Herrnsdorf, H. Chun, G. Faulkner, H. Haas, I.M. Watson, D. O'Brien, M.D. Dawson, A review of gallium nitride LEDs for multi-gigabit-per-second visible light data communications, *Semicond. Sci. Technol.*, 32 (2017) 023001.
- [5] G. Fasol, Room-temperature blue gallium nitride laser diode, *Science*, 272 (1996) 1751-1752.
- [6] T. Melo, Y. Hu, C. Weisbuch, M. Schmidt, A. David, B. Ellis, C. Poblenz, Y. Lin, M. Krames, J. Raring, Gain comparison in polar and nonpolarsemipolar gallium-nitride-based laser diodes, *Semicond. Sci. Technol.*, 27 (2012) 024015.
- [7] A. Udabe, I. Baraia-Etxaburu, D.G. Diez, Gallium nitride power devices: a state of the art

review, *IEEE Access*, 11 (2023) 48628-48650.

[8] K. Peng, S. Eskandari, E. Santi, Characterization and modeling of a gallium nitride power HEMT, *IEEE Transactions on Industry Applications*, 52 (2016) 4965-4975.

[9] A.A. Fletcher, D. Nirmal, A survey of Gallium Nitride HEMT for RF and high power applications, *Superlattices Microstruct.*, 109 (2017) 519-537.

[10] S. Li, A. Waag, GaN based nanorods for solid state lighting, *J. Appl. Phys.*, 111 (2012).

[11] S. Nakamura, Current status of GaN-based solid-state lighting, *MRS Bull.*, 34 (2009) 101-107.

[12] A. Lidow, M. De Rooij, J. Strydom, D. Reusch, J. Glaser, *GaN transistors for efficient power conversion*, John Wiley & Sons, 2019.

[13] A. Lidow, J. Strydom, R. Strittmatter, C. Zhou, GaN: A Reliable Future in Power Conversion: Dramatic performance improvements at a lower cost, *IEEE Power Electronics Magazine*, 2 (2015) 20-26.

[14] W.-S. Choi, J.-Y. Kim, J.-H. Lee, S.-H. Choi, 6G Technology Competitiveness and Network Analysis: Focusing on GaN Integrated Circuit Patent Data, *Journal of Industrial Convergence*, 21 (2023) 1-15.

[15] T.K. Sahu, S.P. Sahu, K. Hembram, J.-K. Lee, V. Biju, P. Kumar, Free-standing 2D gallium nitride for electronic, excitonic, spintronic, piezoelectric, thermoplastic, and 6G wireless communication applications, *NPG Asia Mater.*, 15 (2023) 49.

[16] I. Guy, S. Muensit, E. Goldys, Extensional piezoelectric coefficients of gallium nitride and aluminum nitride, *Appl. Phys. Lett.*, 75 (1999) 4133-4135.

[17] C.M. Foster, R. Collazo, Z. Sitar, A. Ivanisevic, Aqueous stability of Ga-and N-polar gallium nitride, *Langmuir*, 29 (2013) 216-220.

[18] K.S. Novoselov, A.K. Geim, S.V. Morozov, D.-e. Jiang, Y. Zhang, S.V. Dubonos, I.V. Grigorieva, A.A. Firsov, Electric field effect in atomically thin carbon films, *Science*, 306

(2004) 666-669.

[19] K.K. Kim, H.S. Lee, Y.H. Lee, Synthesis of hexagonal boron nitride heterostructures for 2D van der Waals electronics, *Chem. Soc. Rev.*, 47 (2018) 6342-6369.

[20] K. Zhang, Y. Feng, F. Wang, Z. Yang, J. Wang, Two dimensional hexagonal boron nitride (2D-hBN): synthesis, properties and applications, *Journal of Materials Chemistry C*, 5 (2017) 11992-12022.

[21] G. Cassabois, P. Valvin, B. Gil, Hexagonal boron nitride is an indirect bandgap semiconductor, *Nat. Photonics*, 10 (2016) 262-266.

[22] R. Yang, Y. Fan, Y. Zhang, L. Mei, R. Zhu, J. Qin, J. Hu, Z. Chen, Y. Hau Ng, D. Voiry, 2D transition metal dichalcogenides for photocatalysis, *Angew. Chem.*, 135 (2023) e202218016.

[23] W. Choi, N. Choudhary, G.H. Han, J. Park, D. Akinwande, Y.H. Lee, Recent development of two-dimensional transition metal dichalcogenides and their applications, *Mater. Today*, 20 (2017) 116-130.

[24] Q.H. Wang, K. Kalantar-Zadeh, A. Kis, J.N. Coleman, M.S. Strano, Electronics and optoelectronics of two-dimensional transition metal dichalcogenides, *Nat. Nanotechnol.*, 7 (2012) 699-712.

[25] S. Manzeli, D. Ovchinnikov, D. Pasquier, O.V. Yazyev, A. Kis, 2D transition metal dichalcogenides, *Nature Reviews Materials*, 2 (2017) 1-15.

[26] Z.Y. Al Balushi, K. Wang, R.K. Ghosh, R.A. Vilá, S.M. Eichfeld, J.D. Caldwell, X. Qin, Y.-C. Lin, P.A. DeSario, G. Stone, Two-dimensional gallium nitride realized via graphene encapsulation, *Nat. Mater.*, 15 (2016) 1166-1171.

[27] N.A. Koratkar, Two-dimensional gallium nitride, *Nat. Mater.*, 15 (2016) 1153-1154.

[28] C. Fong, S. Ng, F. Yam, H. Abu Hassan, Z. Hassan, Synthesis of two-dimensional gallium nitride via spin coating method: influences of nitridation temperatures, *J. Sol-Gel Sci. Technol.*,

68 (2013) 95-101.

[29] Y. Jia, Z. Shi, W. Hou, H. Zang, K. Jiang, Y. Chen, S. Zhang, Z. Qi, T. Wu, X. Sun, Elimination of the internal electrostatic field in two-dimensional GaN-based semiconductors, *npj 2D Materials and Applications*, 4 (2020) 31.

[30] X. Cai, S. Deng, L. Li, L. Hao, A first-principles theoretical study of the electronic and optical properties of twisted bilayer GaN structures, *J. Comput. Electron.*, 19 (2020) 910-916.

[31] D. Xu, H. He, R. Pandey, S.P. Karna, Stacking and electric field effects in atomically thin layers of GaN, *J. Phys.: Condens. Matter*, 25 (2013) 345302.

[32] G. Kresse, J. Furthmüller, Efficiency of ab-initio total energy calculations for metals and semiconductors using a plane-wave basis set, *Comput. Mater. Sci.*, 6 (1996) 15-50.

[33] G. Kresse, J. Furthmüller, Efficient iterative schemes for ab initio total-energy calculations using a plane-wave basis set, *Phys. Rev. B*, 54 (1996) 11169.

[34] G. Kresse, D. Joubert, From ultrasoft pseudopotentials to the projector augmented-wave method, *Phys. Rev. B*, 59 (1999) 1758.

[35] J.P. Perdew, K. Burke, M. Ernzerhof, Generalized gradient approximation made simple, *Phys. Rev. Lett.*, 77 (1996) 3865.

[36] P.E. Blöchl, Projector augmented-wave method, *Phys. Rev. B*, 50 (1994) 17953.

[37] S. Grimme, J. Antony, S. Ehrlich, H. Krieg, A consistent and accurate ab initio parametrization of density functional dispersion correction (DFT-D) for the 94 elements H-Pu, *J. Chem. Phys.*, 132 (2010).

[38] S. Grimme, Semiempirical GGA-type density functional constructed with a long-range dispersion correction, *J. Comput. Chem.*, 27 (2006) 1787-1799.

[39] V. Wang, N. Xu, J.-C. Liu, G. Tang, W.-T. Geng, VASPKIT: A user-friendly interface facilitating high-throughput computing and analysis using VASP code, *Comput. Phys. Commun.*, 267 (2021) 108033.

[40] A.K. Augustin Lu, T. Yayama, T. Morishita, M.J. Spencer, T. Nakanishi, Uncovering new buckled structures of bilayer GaN: A first-principles study, *J. Phys. Chem. C*, 123 (2018) 1939-1947.